

Particulate Reshapes Surface Jet Dynamics Induced by a Cavitation Bubble

Xianggang Cheng¹, Xiao-Peng Chen^{1,2*}, Zhi-Ming Yuan³,
Laibing Jia^{3*}

¹School of Marine Science and Technology, Northwestern Polytechnical
University, Xi'an, 710072, China.

²Research & Development Institute of Northwestern Polytechnical
University in Shenzhen, Shenzhen, 518057, China.

³Department of Naval Architecture, Ocean & Marine Engineering,
University of Strathclyde, Glasgow, G4 0LZ, UK.

*Corresponding author(s). E-mail(s): xchen76@nwpu.edu.cn;
l.jia@strath.ac.uk;

Abstract

Liquid jet formations on water surfaces serve as a cornerstone in diverse scientific disciplines, underpinning processes in climatology, environmental sciences, and human health issues. Traditional models predominantly focus on pristine conditions, an idealisation that overlooks common environmental irregularities such as the presence of particulate matter on water surfaces. To address this shortfall, our research examines the dynamic interactions between surface particulate matter and cavitation bubbles using floating spheres and spark bubbles. We unveil five novel jet modes, charting a new trajectory away from classical models and demonstrating the enhanced variability in jet dynamics. We observe that particulates significantly lower the energy threshold for jet formation, showing enhanced sensitivity to the presence of particulates. The phase diagram and analyses illustrate how the interplay between the dimensionless spark bubble depth and the dimensionless chasing time between water and particulate influences the jet modes development, from singular streams to complex cavity forms. These insights not only advance our understanding of jet formation, but also unlock the potential for refined jet manipulation across a broad range of physical, environmental, and medical applications.

Liquid jets, a liquid mass propelled into a stream, play critical roles in a diverse array of natural phenomena and industrial applications, and have been extensively studied[1–5]. From influencing natural processes such as cloud formation[6, 7] and aerosol generation[8, 9] to being pivotal in inkjet printing technologies[10–12] and medical aerosol drug delivery systems[13, 14], their significance in a broad range of climatological and environmental sciences, advanced manufacturing, and human health issues is well recognised.

Numerous studies have explored how jets are formed from clean water surfaces, particularly in the context of bubbles’ bursting and splashing phenomena near a free surface[15–18]. The contributions of bubbles in jet formations, considering finite-time singularities, inertial flow focusing, and Rayleigh-Taylor instability, are examined[19–21]. Despite this, a comprehensive understanding of liquid jets in particulate-rich environments[22–25], a scenario commonly encountered in real-world settings, remains surprisingly nascent.

Recently, liquid jets from contaminated water surfaces have been recognised as a global human health issue that relates to the dispersal of pollutants and pathogens[26, 27]. A few researchers have explored the impact of nano- and micro-particles mimicking ocean pollutant particles such as microplastics, bacteria, and viruses on bursting bubbles, focusing on the particles’ transport and accumulation into the jet tip and the succeeding ejected airborne droplets[28–30]. Nonetheless, these investigations often overlook the dynamic and sensitive interplay between particulate matter and jet formations, operating under the assumption that particles on the nano- or micro-scale have minimal influence on jet dynamics. However, this assumption may not be applicable to particles larger than hundreds of microns. Unlike smaller particles, these larger particles substantially contribute to surface defects and create unique interactions within these defects, potentially leading to a profound impact on jet dynamics. The lack of attention to larger particles in current models[16, 18] thus represents a notable gap in our understanding of jet dynamics, especially under realistic and often imperfect environmental conditions.

Existing studies have investigated underwater particles driven by a cavitation bubble[31, 32]. It is found that the driving force originates from either the liquid inertia or bubble contact on one side of the particle. The studies provide valuable insights for our research on how cavitation bubbles interact with particles on water surface.

To address the impact of larger floating particulates on surface jet dynamics, we designed an approach employing solid spheres to create surface imperfections and utilising underwater spark cavitation bubbles to drive jet formations (see Fig. 1a). This approach facilitates an in-depth investigation into the dynamic interplay between spark bubbles and surface defects induced by the spheres.

Here, we found that jet formation is reshaped by the presence of particulates on the water surface. The particulate matter induces enhanced variability in jet dynamics. It also significantly lowers the energy requirement for jet formation, highlighting the system’s sensitivity to particulate presence. By modelling the reaction of the water surface and sphere to the spark bubble’s impact with two key dimensionless numbers, we capture the fluid’s adaptive response to particulate disturbances. Our findings have implications for refined jet manipulation across a broad range of applications,

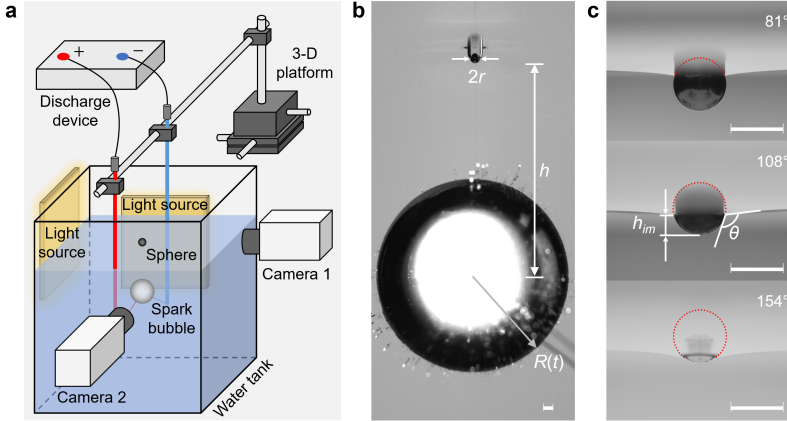


Fig. 1 Experimental setup. **a**, A sketch of the experimental setup. The spark bubble was generated by a low-voltage discharge method, and a surface defect was created by floating a sphere on the water surface. Two high-speed cameras were used to capture the evolution of the water surface and the underwater spark bubble, respectively. **b**, A solid sphere with a radius of r creates a defect when floated on the water surface. The underwater spark bubble is at a distance h below the initial water line, with its instantaneous radius $R(t)$. The interaction causes an upward deformation of the water surface, forming a pit over the sphere. **c**, Underwater close-up of three copper spheres ($r = 500 \mu\text{m}$) resting on still water with varying contact angles ($\theta = 81^\circ$, 108° , and 154°), outlining differences in immersed depths (h_{im}). The red dotted lines outline their emerged parts above the water surface. All scale bars represent 1 mm.

including aerosol production, pollution management, and the control of pathogens' transmission.

Results

Jet modes

We utilise underwater spark bubbles to drive jet formations on the water surface and employ floating solid spheres to create surface defects (Fig. 1a and Methods). Figure 1b outlines the key geometric relationships in the experimental setup. A sphere, serving as a model for particulate matter, is placed on the water surface to create a surface defect. In our experiments, the sphere's radius r ranges from 100 to 2500 μm . The density ratio between the sphere and water, $\rho = \rho_s/\rho_l$, varies between 1.4 and 8.5. The sphere's contact angle with water θ ranges from 81° (hydrophilic) to 154° (superhydrophobic). These physical parameters are detailed in Table 1. The balance among gravity, surface tension, and buoyancy keeps the sphere afloat on the water surface[22]. The sphere's immersed depth h_{im} is determined by r , ρ_s , θ , ρ_l , and the water's surface tension σ [22]. Here, h_{im} ranges from $0.10r$ to $1.55r$. Figure 1c shows how h_{im} varies with θ .

In this study, the maximum radius of the spark bubble is $R_m = 9.2 \pm 0.5$ mm. Here, ± 0.5 is the standard deviation (SD) of the mean for the measured R_m . R_m is selected

Table 1 Physical properties of spheres.

Material	ρ	θ ($^\circ$)		
		hydrophilic	hydrophobic	super-hydrophobic
H62 copper	8.5	81.2 \pm 3.7	108.8 \pm 3.4	155.3 \pm 9.9
304 stainless steel	7.9	-	111.1 \pm 2.2	153.4 \pm 3.9
ZrO ₂	5.9	-	106.2 \pm 1.4	152.7 \pm 5.4
TC4 Ti	4.4	80.8 \pm 1.4	111.2 \pm 1.8	150.8 \pm 8.3
1060 Al	2.7	-	108.7 \pm 1.3	155.8 \pm 6.8
SiO ₂	2.5	-	105.0 \pm 2.3	156.6 \pm 1.0
POM	1.4	82.1 \pm 6.0	-	150.5 \pm 4.2

ρ is relative density, and θ denotes contact angle. The values of \pm represent the standard deviation (SD).

as the characteristic length. A dimensionless depth of the spark bubble is obtained:

$$\hat{h} \equiv \frac{h}{R_m}, \quad (1)$$

where h denotes the initial depth of the spark bubble centre. \hat{h} plays a pivotal role in the formation of free surface jets[17, 18].

Furthermore, we define four critical moments during the oscillations of a spark bubble,

- $t = 0$: The moment when the spark bubble is ignited.
- $t = \tau$: The moment when the spark bubble reaches its maximum radius, R_m .
- $t = T_1$: The moment marking the end of the spark bubble's first oscillation.
- $t = T_1 + T_2$: The moment marking the end of the spark bubble's second oscillation.

τ is selected as the characteristic time. Based on the Rayleigh-Plesset equation for spherical bubbles[33], $\tau \propto R_m$, and $T_1 = 2\tau$. They are constant with a fixed R_m . The presence of the water surface accelerates the collapsing of the spark bubble[17]. In our experiments, $T_1 = (1.9 \pm 0.1 \text{ (SD)})\tau$.

With a sphere floating on the water surface, we observed diverse and distinct jetting phenomena compared to those from flat water surfaces (Fig. 2). Figure 2a serves as reference, which depicts jet formations from flat water surfaces. In scenarios with a flat water surface, underwater spark bubbles induce dynamic pressure variations, leading to multiple jet responses on the free surface[17, 18]. Experiments show that within $0.4 \leq \hat{h} \leq 1.2$, the water surface above the bubble deforms outward, forming a pronounced jet at T_1 (Fig. 2a-I). The bubble rebounds after T_1 and a crown forms from the base of the jet. When $\hat{h} > 1.2$, the water surface rises slightly (Fig. 2a-II). A hump forms without significant jet generation. At $\hat{h} < 0.4$, the bubble breaks the surface, causing water to splash[18], a phenomenon not central to our study's focus on jet formations.

Our research identified five distinct jet modes resulting from the interactions between floating spheres and underwater spark bubbles (Fig. 2b). These modes are named: Tiered Jet (I), Jet Cavity (II), Ventilation (III), Sealed Cavity (IV), and Open

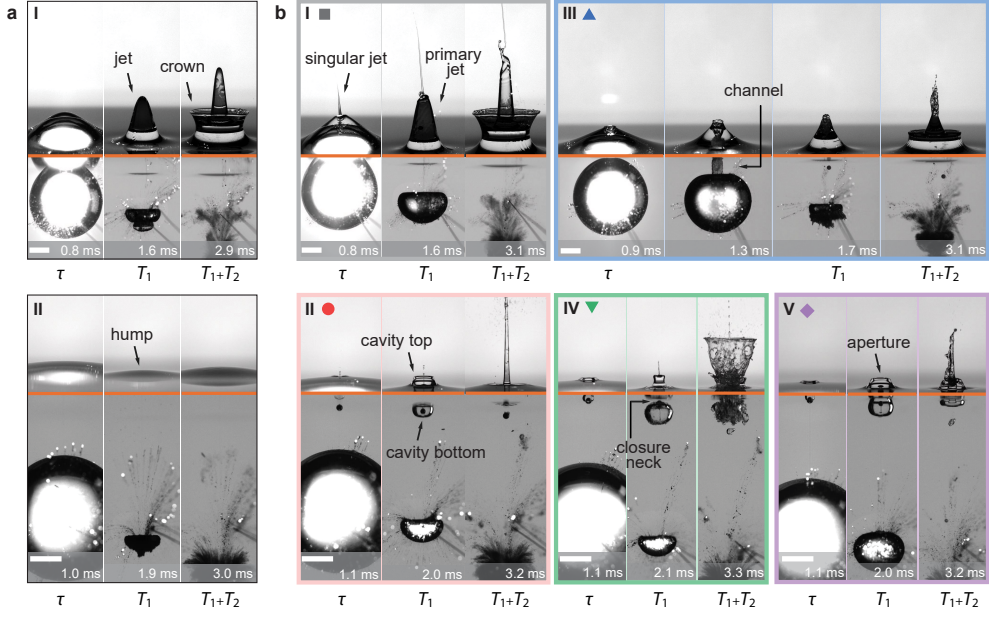


Fig. 2 The snapshots for different jet modes. τ is the duration from the spark bubble's inception to its maximum radius, T_1 and T_2 are the periods of the spark bubble's first and second oscillation, respectively. The orange lines separate the views above and below the waterline. All scale bars represent 5 mm. **a**, Reference group showing the deformation of flat water surfaces. I: Jets development from a flat water surface ($\hat{h} = 0.82$). II: A hump development from a flat water surface ($\hat{h} = 1.57$). **b**, Five jet modes with spheres setting on water surfaces. The spheres radii, $r = 500 \mu\text{m}$. I: Tiered Jet Mode ($\hat{h} = 0.81$, $\rho = 4.4$, $\theta = 80.8^\circ$). II: Jet Cavity Mode ($\hat{h} = 1.62$, $\rho = 4.4$, $\theta = 80.8^\circ$). III: Ventilation Mode ($\hat{h} = 1.00$, $\rho = 1.4$, $\theta = 82.1^\circ$). The second snapshot shows a channel formed between spark bubble and atmosphere. IV: Sealed Cavity Mode ($\hat{h} = 1.93$, $\rho = 4.4$, $\theta = 111.2^\circ$). V: Open Cavity Mode ($\hat{h} = 2.25$, $\rho = 4.4$, $\theta = 111.2^\circ$). The five jet modes are represented by grey squares, red circles, blue upward triangles, green downward triangles, and purple diamonds. Supplementary Videos 1-5 provide further details, showcasing the five jet modes with their corresponding particle-free cases for reference.

Cavity (V). The names are based on the jets' features showing in the second snapshots of each sub-figure in Fig. 2b.

In Mode I, a rapid singular jet and an underlying water bulge form as the spark bubble expands ($t = \tau$). A tiered jet structure is observed with a fine singular jet [19] above the primary jet ($t = T_1$). After the spark bubble rebounds, a crown forms, similar to scenarios without particles as shown in Fig. 2a-I.

In Mode II, a concavity develops at $t = \tau$, surrounding a singular jet at its centre. The concavity enlarges into a cavity as the spark bubble collapses, then it extends to the sphere at T_1 . This configuration, where the sphere is surrounded by an open cavity with a singular jet above it, is defined as the Jet Cavity Mode. Upon the bubble's rebound, the open cavity collapses, ejecting a focused primary jet.

In Mode III, the concavity on the water surface expands as the spark bubble collapses. Its bottom reaches the upper wall of the spark bubble, then forms a channel that bridges the bubble with the atmosphere. This channel facilitates aerodynamic

interaction and creates a ventilation effect. The channel then pinches off, trapping some air in the primary jet and fragmenting it into tiny bubbles ($t = T_1$). After the spark bubble rebounds, a crown forms from the base of the primary jet. The main feature of Mode III is the presence of the channel and the corresponding ventilation phenomenon. Fig. 2b-III shows a case without a singular jet at $t = \tau$. However, it should be noted that in Mode III, we observed both cases with and without singular jets during the spark bubble’s expanding phase ($t \leq \tau$).

A non-axisymmetric wavy feature has been observed in the primary jet of Mode III after $t = T_1 + T_2$ in the Supplementary Video 3. The instability of a jet and its subsequent breakup into droplets or waves is a complex interaction of surface tension, aerodynamic forces, and initial disturbances[34]. In Mode III, high-speed airflow rushes into the spark bubble, followed by the pinch-off of the channel, introducing strong disturbances on the channel wall. Additionally, random factors such as fragmented air bubbles and the horizontal motion of the sphere exist. These result in sinuous wave shape of the jet.

In Modes IV and V, no singular jet forms before $t = \tau$. In Mode IV, as the spark bubble collapses, the expanding cavity seals at its rim. An underwater air bubble is trapped around the sphere. The closure neck is marked in Fig. 2b-IV. A water column and a singular jet above it are formed as the cavity seals. After the spark bubble rebounds, a crown forms from the base of the water column, and the underwater air bubble oscillates strongly. In Mode V, the cavity remains open at $t = T_1$. Its aperture is marked in Fig. 2b-V. Similar to Mode II, the open cavity collapses and generates a focused primary jet as the spark bubble rebounds.

The structures of the five jet modes represent significant departures from the reference jet profiles observed in particle-free cases (Fig. 2), highlighting the enhanced variability in liquid jet dynamics due to particulate interactions. Supplementary Videos 1-5 provide further details, showcasing the five jet modes alongside their corresponding particle-free cases for reference.

Further, we measured the featured geometries of the jets and cavities from typical examples of five jet modes. Their positions and velocities are illustrated in Fig. 3. The initial water level serves as the base line in measuring the vertical locations, z , which is normalised by R_m . The time, t , is normalised by τ . Velocities are normalised by the characteristic velocity V_b ($V_b = R_m/\tau \approx 10.8$ m/s, see Methods). For comparison, the results of jet/hump formation on flat water surfaces at the same \hat{h} are also presented.

As shown in Fig. 3a-e, the plots of singular jet, primary jet, and crown appear approximately linear. We applied linear fittings to these curves to determine corresponding velocities. The velocity of humps is averaged over the interval $t = 0$ to T_1 . Velocities of cavity tops and bottoms are averaged from $t = \tau$ to T_1 . These velocities are plotted in Fig. 3f, corresponding to the cases shown in Fig. 3a-e.

In Fig. 3a, the jet kinematics for Mode I resemble those of the corresponding reference case without a particle at the same \hat{h} . A primary jet forms after spark bubble ignition, and a crown generates after T_1 . Velocities of the primary jet and crown are slightly greater than the reference. Unique to this mode is a fine singular jet immediately after ignition. This jet, with a small amount of mass, moves at a high

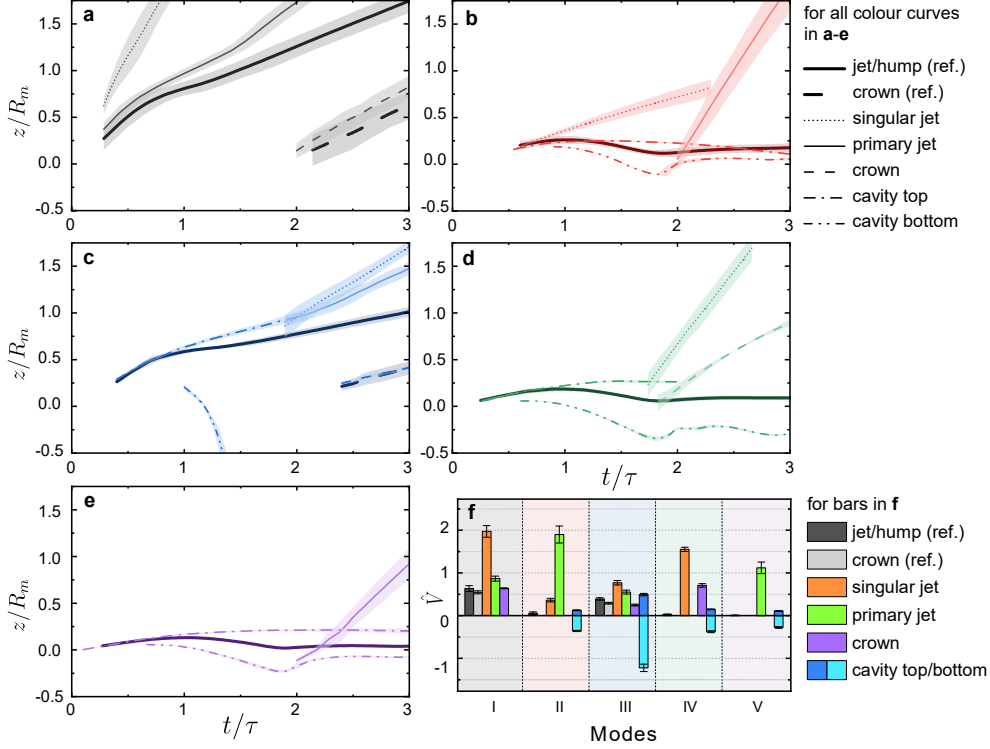


Fig. 3 Positions and velocities of jets and cavities in five jet modes. a-e. The positions of featured geometries in jet formation, including the tips of singular and primary jets, the up edge of crowns, and the cavities' top and bottom. The top of jet/hump from flat water surfaces at the same \hat{h} are included as reference. Positions z are normalised by R_m , and t is normalised by τ . The lines represent the average results from three experimental runs under the same conditions, with shadows around the lines representing the experimental uncertainty. The spheres radii, $r = 500 \mu\text{m}$. The values of \pm represent the standard deviation (SD). **a**, I: Tiered Jet ($\hat{h} = 0.82 \pm 0.01$, $\rho = 4.4$, $\theta = 80.8^\circ$). **b**, II: Jet Cavity ($\hat{h} = 1.57 \pm 0.05$, $\rho = 4.4$, $\theta = 80.8^\circ$). **c**, III: Ventilation ($\hat{h} = 1.03 \pm 0.04$, $\rho = 1.4$, $\theta = 82.1^\circ$). **d**, IV: Sealed Cavity ($\hat{h} = 1.92 \pm 0.07$, $\rho = 4.4$, $\theta = 111.2^\circ$). **e**, V: Open Cavity ($\hat{h} = 2.25 \pm 0.04$, $\rho = 4.4$, $\theta = 111.2^\circ$). **f**, The velocities of jets and cavities in the five modes, normalised by the characteristic velocity of the spark bubble ($V_b = R_m/\tau \approx 10.8 \text{ m/s}$), are presented. The velocities and their standard deviations are calculated from the position measurements in **a-e**.

velocity, approximately twice as fast as the primary jet and three times the speed of the jet in the reference case (Fig. 3f).

Figure 3b shows that Mode II features a high-speed primary jet after T_1 . The jet velocity is comparable to that of the singular jet in Fig. 3a, but with a much larger mass. This primary jet originates from the collapsing cavity bottom after T_1 . Its high speed results from flow-focusing at the curved interface, where kinetic energy is focused[20]. In contrast, the corresponding reference case shows only a hump with no jet ejection.

In Fig. 3c, the cavity bottom exhibits rapid downward movement, showing the highest speed among all cases in Fig. 3. This movement leads to the formation of a

channel between the spark bubble and the atmosphere, distinguishing Mode III from other modes.

Figure 3d corresponds to Mode IV. A singular jet is generated from the cavity top at the time the cavity seals. The sealed air in the cavity maintains the position of the cavity bottom with fluctuations after T_1 . In Fig. 3e, a primary jet forms from the cavity bottom after T_1 . The curves are reminiscent of those in Fig. 3b, except there is no singular jet.

Key moments in jet formation observed in Fig. 3 include τ and T_1 . The singular jets in Modes I and II are generated before $t = \tau$. While in Modes III and IV, when the cavities close up just before $t = T_1$, they will also generate singular jets from the top of the cavities. In Modes II-V, cavities appear on the water surface. Their top and bottom velocities vary. After T_1 , high-speed primary jets are generated from the collapsed cavity bottom in Modes II and V. Crowns also form in Modes I, III and IV after T_1 .

Figure 3 shows the variation of jet and cavity kinematics with the presence of spheres floating on the water surface. The interaction between a surface defect from a floating sphere and the underwater spark bubble leads to increased variability in jet types and enhanced jet velocity, compared to scenarios without a sphere.

Modes evolution and distribution

To further illustrate how surface defects from a floating sphere lead to varied jet modes, we draw a schematic depicting their temporal evolution, as shown in Fig. 4. When a spark ignites near a sphere, a pit forms over the sphere due to the differential ascent caused by the density difference between the sphere and water. The surrounding water reacts in one of two ways: it either quickly gathers over the sphere, sealing the pit and generating a singular jet, or responds more slowly, leaving the pit open.

In the scenario where the pit seals quickly (lower branch), a fine singular jet is emitted along with the growth of a water bulge driven by the expansion of the spark bubble. As the singular jet matures, a concavity emerges at its base ($t = \tau$). The concavity expands into a cavity during the collapsing phase of the spark bubble. This branch further divides into three distinct modes: in Mode I, the cavity does not reach the sphere; in Mode II, the cavity deepens and reaches the sphere; and in Mode III, the cavity extends beyond the sphere, reaches the upper wall of the spark bubble, and forms a channel.

Alternatively, in the scenario where the pit remains open (upper branch), the pit evolves into an expanding cavity as the spark bubble collapses. This routine also branches into three modes: in Mode III, the cavity deepens and reaches the spark bubble, forming a channel; in Mode IV, the cavity expands and gets sealed; and in Mode V, the cavity expands but remains open.

Both the upper and lower branches can evolve into Mode III, characterised by a channel connecting the spark bubble to the atmosphere. But in the lower branch, a singular jet is observed above the open channel.

At time T_1 , and later at $T_1 + T_2$, these processes evolve into the snapshots shown in Fig. 2. These diverse phenomena and various jet modes originate from interactions between surface defects induced by floating particles and underwater spark bubbles.

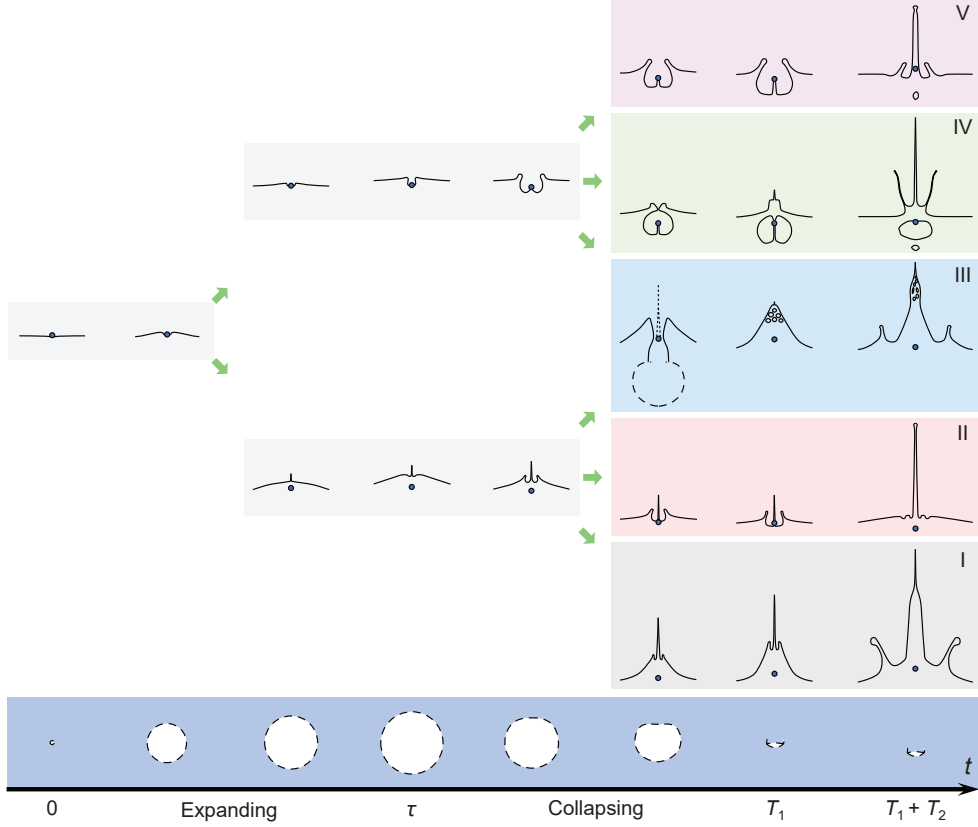


Fig. 4 A schematic of temporal evolution for five jet modes. The bottom row with a light blue background illustrates the temporal evolution of the spark bubble during its first two oscillation periods. This sequence begins with the spark ignition at $t = 0$, progresses through the expanding stage to the maximum radius at τ , then to the first collapse at T_1 , and continues into the next oscillation period until the second collapse at $T_1 + T_2$. The dashed line represents the outlines of the spark bubble. The upper plots illustrate the evolution of surface defects. They are scaled up for a clear view. The blue circles represent the spheres, and the solid lines represent the air-water interfaces. As time progresses from left to right, it branches from a sphere resting on the water surface to five jet modes, depicting against grey, red, blue, green, and purple backgrounds, respectively.

The temporal evolution of these jets initiates with upward water movements, branching into one of five distinct modes. This underscores the substantial impact of surface particulates on shaping liquid behaviour and uncovering complex fluidic responses.

Building on the observations of these diverse jet modes and their formations, our study advances to identify crucial factors governing jet formation. The jet formation is driven by the underwater spark bubble. The mechanical energy of a spark bubble is determined by its volume and the driving pressure. Theoretically, it can be expressed as $E = \frac{4}{3}\pi R_m^3 (p_{atm} - p_v)$, where p_{atm} and p_v are the atmosphere pressure and the saturated vapour pressure of water, respectively[17]. The driving energy E is initially stored as pressure potential energy, associated with the work done by the radiated pressure from the spark bubble, which deforms the water surface and initiates the jet

motion. The spark bubble ignites at a distance of h from the water surface and sphere. The radiated energy density on the water surface can be characterised as,

$$e \sim \frac{E}{4\pi h^2} \propto \hat{h}^{-2}. \quad (2)$$

The dimensionless depth of the spark bubble, \hat{h} , serves as a key dimensionless number reflecting the energy density on the water surface radiated by the spark bubble (Eq. 1). It determines the amplitude of the alternating driving pressure throughout the jet formation.

The sphere setting on the water surface is a unique component in this study. The interaction between the sphere and water, including factors such as the sphere's radius, density, and contact angle, as well as the water's density, surface tension, and viscosity, represents a complex interplay. To simplify the consideration of the physical processes involved, we focus on the initial branching of modes shown in Fig. 4, specifically on whether a singular jet is generated during the spark bubble's initial expanding stage ($0 < t < \tau$).

Here we define a 'chasing time', the duration required for the water surface to catch up with and cover the unimmersed portion of the floating sphere, $t_c^u = (2r - h_{im})/(V_l - V_s)$, where V_l and V_s are the characteristic velocities of the water surface and the sphere, respectively. Based on energy and volume conservation, V_s and V_l can be estimated as $V_s = \rho^{-\frac{1}{2}}V_l$, $V_l = V_b/\hat{h}^2$. Furthermore, by normalising with the time scale of the spark bubble, τ , a dimensionless chasing time is obtained:

$$t_c = \frac{t_c^u}{\tau} = \frac{(2 - \hat{h}_{im})\hat{r}}{1 - \rho^{-\frac{1}{2}}}\hat{h}^2, \quad (3)$$

where \hat{h}_{im} represents the dimensionless immersed depth of the sphere (see Fig. 1c), $\hat{h}_{im} = h_{im}/r$; and \hat{r} denotes the radius ratio between the sphere and the spark bubble, $\hat{r} = r/R_m$. t_c serves as the other key dimensionless number, showing the dynamics of how the water surface and the sphere respond to the spark bubble during the initial phase. It is influenced by sphere properties, surface dynamics, and the strength of the spark bubble.

We carried out a systematic study of surface jet dynamics using spheres with varying properties. The spheres' radii range in $100 \sim 2500 \mu\text{m}$, relative densities range from 1.4 to 8.5, and wetting abilities from hydrophilic to super-hydrophobic (Tab. 1). This study focuses on the jet dynamics induced by a spark cavitation bubble with a floating sphere on the water surface. We observed that the spark bubble directly contacted the sphere in a few experiments. These bubble contacts are a different driven mechanism from the liquid inertia driven ones[32], and thus are not included in the analysis presented here.

The jet modes are categorised in the phase diagram, as depicted in Fig. 5a. When a sphere is present on the water surface, a jet forms even as \hat{h} reaches 3.5 (Mode V in Fig. 5a), exceeding the typical upper boundary of $\hat{h} \approx 1.2$ for jet formation on a flat water surface[17, 18]. With the sphere, the energy density on the water surface

bubble's expansion. Due to density differences, the water surface moves faster than the sphere ($V_i/V_s \sim \rho^{\frac{1}{2}}$).

During the expanding phase of the spark bubble ($t \leq \tau$), mode differentiation is primarily determined by t_c . The variation in t_c results in two scenarios: a smaller t_c results in the pit sealing and the ejection of a singular jet (②), whereas a larger t_c leads to pit opening (③). In our experiments, the horizontal boundary line at $t_c \approx 0.2$ was observed.

In the following collapsing phase of the spark bubble ($\tau < t < T_1$), the interface differences become more pronounced, further evolving into five distinct jet modes. In scenario ②, the water bulge keeps moving upward, while the concavity at the junction between the singular jet and the water bulge moves downward and develops into a cavity (④). The evolution is driven by the negative radiated pressure from the spark bubble. The positions of the concavity and the sphere, and the moving speed of the water surface at the cavity, are determined by \hat{h} . Depending on the positions of the water surface, sphere, and spark bubble, and the moving speed of the water surface, the jet develops into Mode I, II or III.

In scenario ③, the pit expands into a cavity as the spark bubble collapses. If the bottom of the cavity moves fast enough to reach the upper wall of the spark bubble, the jet evolves into Mode III. Otherwise, the cavity enlarges gradually and results in Mode IV or V.

Air flows into the cavity as it expands (⑤). The airflow rushing into the cavity induces an aerodynamic pressure difference across the cavity rim, $\Delta p \propto -\rho_a V_a^2$, where V_a is the airflow speed and ρ_a is the air density. This pressure difference drives the collapse of the cavity rim, similar to the surface seal phenomenon observed in water entry problems [35, 36]. If the collapse duration of the cavity rim is less than or equal to that of the spark bubble, the cavity seals before the bubble rebounds, resulting in Mode IV. Otherwise, the cavity remains open at $t = T_1$, resulting in Mode V. The collapse duration of the cavity rim is determined by Δp , which depends on the airflow speed V_a . Based on the geometric relationship between the cavity rim and the cavity, V_a is related to the downward speed of the cavity bottom, primarily determined by the dimensionless spark bubble depth \hat{h} . This indicates a critical value of \hat{h} that determines whether the cavity is sealed or not, consistent with experimental findings where the vertical line at $\hat{h} \approx 2.1$ marks the boundary separating Mode V from Mode IV.

Mode III occurs at a small \hat{h} and a large t_c . The boundaries around Mode III include a vertical line between Modes III and IV, and an oblique line between Modes III and I. The vertical boundary is primarily determined by the strength of the spark bubble. A smaller \hat{h} results in Mode III, while a larger \hat{h} leads to Mode IV.

The boundary between Modes III and I is a straight oblique line on the log-log plot, indicating a power-law relationship expressed as $t_c = k\hat{h}^n$. With n as the slope and $\log(k)$ as the intercept. We find $n = 2$ on the plot. Considering the definition of t_c in Eq. 3, the intercept $\log(k)$ is independent of \hat{h} . Thus, both the slope and intercept of the line do not depend on \hat{h} , suggesting that the boundary between Modes III and I is independent of \hat{h} .

The key dimensionless number t_c captures the competitive motions of the water surface and the sphere during the first expansion phase of the spark bubble. The

horizontal line at $t_c \approx 0.2$ separates the branches with and without singular jets as the spark bubble expands. Experiments below the line exhibit singular jets before $t = \tau$, depicted as I, II and III.a in Fig. 5b. Conversely, when above the line, no singular jet forms before $t = \tau$, shown as III.b, IV and V.

However, several experiments of Mode V appear below the line $t_c \approx 0.2$. To understand this exception, we examined the experiments and found that the spheres' radii are $r \leq 175 \mu\text{m}$. Three dimensionless numbers, the capillary number $Ca = \mu V_l / \sigma$ (μ is the viscosity of water), the Reynolds Number $Re = \rho_l V_l r / \mu$, and the Weber number $We = \rho_l V_l^2 r / \sigma$, were calculated to evaluate the contribution of surface tension, viscous and inertial forces. For $r = 100 \sim 175 \mu\text{m}$ and $1.6 < \hat{h} < 2.8$, we have $Ca < 0.06$, $Re > 137$, and $We = 3 \sim 43$. The values of Ca and Re indicate that viscous forces can be neglected compared to surface tension and inertial forces. The value of We suggests that surface tension effects should be considered for sufficiently small spheres, a factor not taking account in our current physical model. The omission of surface tension effects for small-radii spheres underestimates their velocities, thereby reducing their chasing times t_c . Moreover, strong surface tension effects also prevent the formation of rims at the cavity apertures, thereby keeping the cavities open.

Conclusion and Discussion

In summary, our study reveals that surface jet dynamics are more complex and sensitive to particulates than previously understood. The presence of particulates on the water surface induces surface defects. The interaction between the underwater spark bubbles, water surface defects, and spheres reshapes the jet dynamics. We observed five new jet modes, showing enhanced variability in jet types. Moreover, the jet velocities are increased, and the effective range of the spark bubble's dimensionless depth for jet formation is extended. These illustrate that the presence of particulates reduces the energy required for jet formation, and exhibits an enhanced responsiveness of the water surface.

We introduced two key dimensionless numbers, including the spark bubble's dimensionless depth \hat{h} , and the dimensionless chasing time t_c between the water and sphere. They determine the evolution of the water surface from a defect induced by a floating sphere to diverse jetting modes. \hat{h} reflects the energy density on the water surface radiated by the spark bubble. It determines the amplitude of the alternating driving pressure throughout the jet formation. t_c captures the competitive movement between the water surface and the sphere during the first expanding phase of the spark bubble. It relies on the properties of spheres and the liquid, and the energy density at the sphere location.

Despite the overall complexity of the physical picture, our proposed model, based on the two key dimensionless numbers, was applicable across most experimental conditions in this study. In this study, the surface evolution is dominated by inertial forces and can be classified as liquid inertia driven. This simplifies the analysis of the physical processes. In the first expanding phase of the spark bubble, the evolution of the surface defect is primarily affected by the velocity difference between the solid and liquid, which determines whether a singular jet is formed. During the collapsing

phase of the spark bubble, inertial effects are mainly reflected in two aspects: 1) the growth of the cavity under the impact of the collapsing spark bubble, and 2) the pressure difference across the cavity rim induced by the airflow rushing into the cavity. The contribution of surface tension is only considered in estimating the defect size. Both it and viscosity are not taken into account in the dynamic evolution of the water surface. This oversight limits the applicability of the key dimensionless numbers for small-radius spheres.

This investigation provides a foundation for understanding the interactions between floating particulates and surface jets, paving the way for more detailed future studies. The enhanced variability and sensitivity of surface jet dynamics in the presence of particulates bridge a gap in existing fluid dynamic theories. This discovery provides new strategies to suppress aerosol generation by removing particles and to enhance jet formation by introducing particles or other small foreign bodies on the water surface. These advancements in understanding have practical implications across diverse fields.

In environmental science, our findings shed new light on how particulate matter influences water jet behaviours. For instance, microplastics floating on the sea surface could enhance the formation of spray aerosols, potentially releasing pollutants or pathogens into the atmosphere. Understanding these dynamics is crucial for mitigating environmental impacts and safeguarding aquatic ecosystems.

In the field of medical engineering, this study offers insights for advancing aerosol drug delivery systems. Particulates enhance the variability and sensitivity of jet formation, presenting opportunities for more efficient aerosol generation with reduced energy input. Additionally, the generation of high-speed primary jets can be applied to needle-free drug delivery techniques.

Methods

Experimental setup

The experimental apparatus was constructed for observations of the interplay between an underwater spark bubble and a floating sphere on the water surface (Fig. 1a). The setup is placed on an optical table. The principal components of the setup comprised the following elements:

- **Water tank:** A transparent acrylic tank was employed, with dimensions of $25 \times 25 \times 30$ cm³. It is filled with deionised water to a depth of 25 cm.
- **Discharge electrodes:** Copper wires with a diameter of 60 μ m were used as electrodes to create the spark bubbles. These were manipulated with a three-dimensional platform for positioning.
- **Sphere positioning:** The spheres were initially picked up with a tweezer and gently placed on the water surface. To fine-tune their position, a rubber suction bulb was used, which allowed for control by gently blowing air. We used the feedback from the high-speed camera to monitor and adjust the position to be straight above the contact point of the copper wires. This method minimises the drift of a sphere from the desired location prior to the commencement of each experiment.

- **High-speed imaging:** Two high-speed cameras (Phantom VEO 711, Vision Research Inc., USA) equipped with parallel back lighting were utilised to capture the interaction process. The cameras were set orthogonal to each other to record the front and side views of the surface defect evolution and the underwater spark bubble behaviour, respectively. The framerate was set at between 7500 and 60,000 frames per second, with an exposure time ranging from 5 to 20 μs .
- **Ambient condition:** The water tank was placed in an ambient with a temperature consistent at around 25°C for 24 hours before conducting experiments.
- **Data acquisition and analysis:** Matlab build-in image processing and edge detection algorithms were used in measuring the physical quantities. Accuracy in the image analysis was maintained to a single pixel, which correlates to a spatial resolution of 35 μm .

Materials

The experiment employed spheres with radii (r) ranging from 100 to 2500 μm . These spheres, made from different materials, were selected to cover a range of relative densities, $\rho = \rho_s/\rho_l = 1.4 \sim 8.5$, where ρ_s and ρ_l represent the densities of the solid sphere and water, respectively. The materials used for the spheres included H62 copper, 304 stainless steel, zirconia (ZrO_2), titanium alloy (TC4 Ti), 1060 aluminium (1060 Al), silicon dioxide (SiO_2), and polyoxymethylene (POM).

The spheres were prepared with a cleaning process for experiments. They were ultrasonically cleaned in acetone, ethanol, and deionised water, lasting 30 minutes for each step. Further, the spheres were coated with different materials to alter their contact angles. To obtain hydrophobic spheres, a fluorinated silane with low surface energy: 1H, 1H, 2H, 2H-perfluorodecyltriethoxysilane (Beijing HWRK Chemical Co., Ltd, China), was deposited onto the sphere surface via evaporative deposition. The super-hydrophobic spheres were fabricated by coating the surface with a thin layer of hydrophobic nano-particles. The cleaned spheres were immersed in the coating liquid (Ultra Glaco, Soft99 Co., Japan). After coating, the spheres were taken out and left to dry naturally for 12 hours, resulting in super-hydrophobic surfaces.

The contact angle, θ , was measured by using a sessile drop method. The values were validated by calculating the force balance in quiescent floating state (Fig. 1c). Table 1 summarises the density and contact angle data for spheres used in the experiments.

Deionised water was used in the experiment, with a density of $\rho_l = 998 \text{ kg/m}^3$, a viscosity of $\mu = 1 \text{ mPa}\cdot\text{s}$, and a surface tension of $\sigma = 72.8 \text{ mN/m}$.

Generation and characterisation of the spark bubble

The low-voltage underwater spark-discharge method was used to generate the spark cavitation bubble[37]. Upon activation of the circuit at $t = 0$, an initial spark at the electrodes' contact point rapidly vaporises the adjacent water, releasing a substantial amount of heat. It leads to the formation of an expanding bubble, driven by the high internal pressure and temperature. Following the spark discharge, the bubble expands to its maximum radius at $t = \tau$, then collapses to its minimum volume at $t = T_1$, and

rebounds, resulting in oscillations. In our experiments, the maximum radius of the spark bubbles is $R_m = 9.2 \pm 0.5$ (SD) mm.

τ is chosen as the characteristic time of the spark bubble, which can be theoretically determined using the Rayleigh-Plesset equation for spherical bubbles[33],

$$\tau \cong 0.915R_m\sqrt{\frac{\rho_l}{p_{atm} - p_v}}, \quad (4)$$

where p_{atm} and p_v are the atmosphere pressure and the saturated vapour pressure of water, respectively. T_1 is theoretically twice as much as τ for spherical bubbles[33]. The presence of the free surface accelerates the collapse of the spark bubble[17]. In our experiments, $T_1/\tau = 1.9 \pm 0.1$ (SD).

Furthermore, the characteristic velocity of the spark bubble is determined as

$$V_b = \frac{R_m}{\tau} \cong \frac{1}{0.915} \sqrt{\frac{p_{atm} - p_v}{\rho_l}}. \quad (5)$$

V_b is independent of the spark bubble's size. By substituting $p_{atm} = 101325$ Pa, and $p_v = 3169$ Pa at 25°C into Eq. 5, we obtain $V_b \approx 10.8$ m/s.

Data availability

The data supporting the findings of this study are available within the paper and its supplementary information files. Additional data related to this paper may be requested from the corresponding author.

References

- [1] Zeff, B. W., Kleber, B., Fineberg, J. & Lathrop, D. P. Singularity dynamics in curvature collapse and jet eruption on a fluid surface. *Nature* **403**, 401–4 (2000).
- [2] Brooks, S. D. & Thornton, D. C. O. Marine aerosols and clouds. *Annual Review of Marine Science* **10**, 289–313 (2018).
- [3] Ji, B., Yang, Z. & Feng, J. Compound jetting from bubble bursting at an air-oil-water interface. *Nature Communications* **12**, 6305 (2021).
- [4] Deike, L. Mass transfer at the ocean–atmosphere interface: The role of wave breaking, droplets, and bubbles. *Annual Review of Fluid Mechanics* **54**, 191–224 (2022).
- [5] Sudduth, E. R., Trautmann-Rodriguez, M., Gill, N., Bomb, K. & Fromen, C. A. Aerosol pulmonary immune engineering. *Advanced Drug Delivery Reviews* **199** (2023).
- [6] Wilson, T. W. *et al.* A marine biogenic source of atmospheric ice-nucleating particles. *Nature* **525**, 234–238 (2015).

- [7] Quinn, P. K., Coffman, D. J., Johnson, J. E., Upchurch, L. M. & Bates, T. S. Small fraction of marine cloud condensation nuclei made up of sea spray aerosol. *Nature Geoscience* **10**, 674–679 (2017).
- [8] Alsved, M. *et al.* Natural sources and experimental generation of bioaerosols: Challenges and perspectives. *Aerosol Science and Technology* **54**, 547–571 (2019).
- [9] Anguelova, M. D. Big potential for tiny droplets. *Nature Geoscience* **14**, 543–544 (2021).
- [10] Modak, C. D., Kumar, A., Tripathy, A. & Sen, P. Drop impact printing. *Nature Communications* **11** (2020).
- [11] Lin, S. J. *et al.* Macrodrip-impact-mediated fluid microdispensing. *Advanced Science* **8** (2021).
- [12] Lohse, D. Fundamental fluid dynamics challenges in inkjet printing. *Annual Review of Fluid Mechanics* **54**, 349–382 (2022).
- [13] Douafer, H., Andrieu, V. & Brunel, J. M. Scope and limitations on aerosol drug delivery for the treatment of infectious respiratory diseases. *Journal of Controlled Release* **325**, 276–292 (2020).
- [14] Biney, I. *et al.* Guidance on mitigating the risk of transmitting respiratory infections during nebulization by the COPD foundation nebulizer consortium. *Chest* (2023).
- [15] Lee, J. S. *et al.* Size limits the formation of liquid jets during bubble bursting. *Nature Communications* **2** (2011).
- [16] Lai, C.-Y., Eggers, J. & Deike, L. Bubble bursting: Universal cavity and jet profiles. *Physical Review Letters* **121** (2018).
- [17] Zhang, S., Wang, S. P. & Zhang, A. M. Experimental study on the interaction between bubble and free surface using a high-voltage spark generator. *Physics of Fluids* **28**, 032109 (2016).
- [18] Kang, Y. J. & Cho, Y. Gravity-capillary jet-like surface waves generated by an underwater bubble. *Journal of Fluid Mechanics* **866**, 841–864 (2019).
- [19] Yang, Z., Ji, B., Ault, J. T. & Feng, J. Enhanced singular jet formation in oil-coated bubble bursting. *Nature Physics* (2023).
- [20] Tagawa, Y. *et al.* Highly focused supersonic microjets. *Physical Review X* **2** (2012).
- [21] Rosselló, J. M., Reese, H., Raman, K. A. & Ohl, C. D. Bubble nucleation and jetting inside a millimetric droplet. *Journal of Fluid Mechanics* **968** (2023).

- [22] Vella, D. Floating versus sinking. *Annual Review of Fluid Mechanics* **47**, 115–135 (2015).
- [23] Li, A. *et al.* Adjustable object floating states based on three-segment three-phase contact line evolution. *Proceedings of the National Academy of Sciences of the United States of America* **119** (2022).
- [24] Gwon, M. *et al.* Scale dependence in hydrodynamic regime for jumping on water. *Nature Communications* **14**, 1473 (2023).
- [25] Protière, S. Particle rafts and armored droplets. *Annual Review of Fluid Mechanics* **55**, 459–480 (2023).
- [26] Sha, B., Johansson, J. H., Salter, M. E., Blichner, S. M. & Cousins, I. T. Constraining global transport of perfluoroalkyl acids on sea spray aerosol using field measurements. *Science Advances* **10**, ead11026 (2024).
- [27] Bourouiba, L. The fluid dynamics of disease transmission. *Annual Review of Fluid Mechanics* **53**, 473–508 (2021).
- [28] Ji, B., Singh, A. & Feng, J. Water-to-air transfer of nano/microsized particulates: Enrichment effect in bubble bursting jet drops. *Nano Letters* **22**, 5626–5634 (2022).
- [29] Dubitsky, L., McRae, O. & Bird, J. C. Enrichment of scavenged particles in jet drops determined by bubble size and particle position. *Physical Review Letters* **130** (2023).
- [30] Harb, C., Pokhrel, N. & Foroutan, H. Quantification of the emission of atmospheric microplastics and nanoplastics via sea spray. *Environmental Science & Technology Letters* **10**, 513–519 (2023).
- [31] Wu, S. J., Zuo, Z. G., Stone, H. A. & Liu, S. H. Motion of a free-settling spherical particle driven by a laser-induced bubble. *Physical Review Letters* **119**, 084501 (2017).
- [32] Ren, Z. B., Zuo, Z. G., Wu, S. J. & Liu, S. H. Particulate projectiles driven by cavitation bubbles. *Physical Review Letters* **128** (2022).
- [33] Franc, J. P. & Michel, J. M. *Fundamentals of Cavitation*, p.36–39 (Springer, Dordrecht, 2005).
- [34] Weber, C. Zum zerfall eines flüssigkeitsstrahles. *ZAMM-Journal of Applied Mathematics and Mechanics/Zeitschrift für Angewandte Mathematik und Mechanik* **11**, 136–154 (1931).
- [35] Aristoff, J. M. & Bush, J. W. M. Water entry of small hydrophobic spheres. *Journal of Fluid Mechanics* **619**, 45–78 (2009).

- [36] Eshraghi, J., Jung, S. & Vlachos, P. P. To seal or not to seal: The closure dynamics of a splash curtain. *Physical Review Fluids* **5** (2020).
- [37] Goh, B. H. T., Oh, Y. D. A., Klaseboer, E., Ohl, S. W. & Khoo, B. C. A low-voltage spark-discharge method for generation of consistent oscillating bubbles. *Review of Scientific Instruments* **84** (2013).

Acknowledgements

X. Cheng and X. Chen acknowledge the support provided by the National Natural Science Foundation of China (grant no. 11872315), the Shenzhen Science and Technology Program (grant no. 2022A1515011201). L. J. thanks the support from the Royal Society Research Fund (RGS\R2\222218). We thank A-Man Zhang and Yunlong Liu at Harbin Engineering University; Erqiang Li at University of Science and Technology of China; Haibao Hu, Hengdong Xi, Xiao Huang and Jun Luo at Northwestern Polytechnical University for helping with our experiments. We acknowledge Chao Sun at Tsinghua University for helpful discussions.

Author contributions

X. Cheng and X. Chen developed the original concept for this study. The design of the experimental procedures was a collaborative effort by X. Cheng, X. Chen, and L. J. X. Cheng carried out the experiments. The analytical phase was conducted jointly by X. Cheng, X. Chen, and L. J. Discussion and interpretation of the results and the manuscript were contributed to the collaborative efforts of X. Cheng, X. Chen, Z. Y., and L. J.

Competing interests

The authors declare no competing interests.

Additional information

Supplementary information including the Supplementary Videos, is available for this paper.

Correspondence and requests for materials should be addressed to X. Chen or L. J.